

# Numerical modeling and experimental validation of passive microfluidic mixer designs for biological applications <sup>EP</sup>

Cite as: AIP Advances **10**, 105116 (2020); <https://doi.org/10.1063/5.0007688>

Submitted: 17 March 2020 • Accepted: 21 September 2020 • Published Online: 07 October 2020

 Shubha Jain and  Harikrishnan Narayanan Unni

## COLLECTIONS

 This paper was selected as an Editor's Pick



View Online



Export Citation



CrossMark

## ARTICLES YOU MAY BE INTERESTED IN

[A “twisted” microfluidic mixer suitable for a wide range of flow rate applications](#)  
Biomicrofluidics **10**, 034120 (2016); <https://doi.org/10.1063/1.4954812>

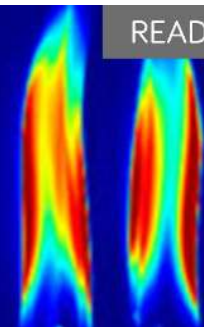
[Enhancement of spin signals by thermal annealing in silicon-based lateral spin valves](#)  
AIP Advances **10**, 095021 (2020); <https://doi.org/10.1063/5.0022160>

[Drying behavior of magnetic nanofluid in ambient conditions](#)  
AIP Advances **10**, 105018 (2020); <https://doi.org/10.1063/5.0019183>

**AIP Advances**

Fluids and Plasmas Collection

READ NOW



# Numerical modeling and experimental validation of passive microfluidic mixer designs for biological applications

Cite as: AIP Advances 10, 105116 (2020); doi: 10.1063/5.0007688  
Submitted: 17 March 2020 • Accepted: 21 September 2020 •  
Published Online: 7 October 2020



Shubha Jain  and Harikrishnan Narayanan Unni<sup>a)</sup> 

## AFFILIATIONS

Department of Biomedical Engineering, Indian Institute of Technology, Hyderabad 502285, India

<sup>a)</sup> Author to whom correspondence should be addressed: [harikrishnan@iith.ac.in](mailto:harikrishnan@iith.ac.in)

## ABSTRACT

The present work reports numerical simulation and experimental validation of novel designs of microfluidic mixers that can be employed for biological mixing applications. Numerical simulations involving various geometrical models were performed for design optimization. The effect of the presence of embedded obstacles was studied in detail, in order to understand the effect of channel occlusion on micromixing. The mixing performance of various channel designs was compared, and crossover in the mixing performance of the designs was observed in response to a change in the flow Reynolds number (Re). The improvement in micromixing efficiency was discussed in connection with the variations in local values of the Reynolds number and Dean number. It was observed that the presence of obstacles contributes to a significant increase in local Re in the vicinity of sharp-edged obstacles, thereby enhancing the efficiency of mixing. In addition, the local Dean number is observed to increase significantly inside spiral microfluidic designs. We validate the optimized microfluidic mixer designs by performing micromixing experiments and image analysis based on regions of interest along the length of the channels. Numerical predictions were observed to be in reasonable agreement with experimental results. Finally, we demonstrated the biological applicability of an optimized micromixer design for on-chip detection of calcium levels in blood serum. The passive mixing designs presented in this work are useful for chip-scale implementations of cell-drug biology, where some of the key cell signaling processes appear at second time scales.

© 2020 Author(s). All article content, except where otherwise noted, is licensed under a Creative Commons Attribution (CC BY) license (<http://creativecommons.org/licenses/by/4.0/>). <https://doi.org/10.1063/5.0007688>

## I. INTRODUCTION

Microfluidic principles are extensively employed in several fields linked to biological and biomedical applications. Microfluidic devices are employed for numerous analytical applications such as bio-sensing,<sup>1</sup> gene amplification,<sup>2</sup> and drug screening.<sup>3</sup> A large number of such implementations require efficient mixing of samples performed *on-chip*. Numerous techniques of microfluidic mixing are reported in the literature that can be broadly categorized as “active mixers” and “passive mixers.”<sup>4–8</sup> Active mixers exploit external energy sources such as thermal,<sup>9</sup> acoustic,<sup>10</sup> magnetic,<sup>11</sup> and electrokinetic<sup>12</sup> sources to improve the mixing efficiency. Passive mixers avoid these complications by incorporating complicated channel geometries so that adequate mixing is achieved

without the use of any external energy sources. Passive mixer designs have advantages of lower cost, less complexity, and ease of fabrication compared to active mixer designs. Microfluidic flows are mostly laminar, and the concepts of fluidic resistance and surface area to volume ratio<sup>13,14</sup> are strongly correlated with the performance of microfluidic mixing devices. Rapid and efficient mixing in microchannels is a challenge because diffusion is an extremely slow process.<sup>15</sup> The Reynolds number (Re) is a characteristic dimensionless number that represents the strength of convective transport to viscous effects. Viscous effects are predominant at low Reynolds numbers.<sup>16,17</sup> The limitation of minimal convective transport can be overcome by making alterations in the channel geometry so that chaotic advection or secondary flow vortices can be induced.

In the past few years, various types of passive microfluidic mixers were proposed by numerous researchers to study micromixing.<sup>18–33</sup> Hossain *et al.*<sup>24</sup> performed numerical simulation on three types of passive micromixers. The results indicated that square wave channels result in better mixing compared to zig-zag and curved channel designs.<sup>24</sup> Buchegger *et al.*<sup>25</sup> designed a horizontal multi-lamination micromixer with wedge-shaped inlet channels. Micro T-mixers were designed, and their feasibility for rapid mixing at low Reynolds numbers was investigated.<sup>30</sup> Li<sup>31</sup> designed a three-dimensional, diagonal ridge micromixer (DRSRM) based on the principle of splitting and recombination and chaotic advection. The diagonal ridge designs presented were responsible for enhancing the mixing performance by stretching and generating vortex flow.<sup>31</sup> Lee *et al.*<sup>32</sup> performed an experimental and numerical investigation of micromixers where the effect of the number and size of elliptic barriers was investigated. Tsai and Wu<sup>33</sup> reported an efficient passive micromixer where multidirectional vortices were generated due to radial baffles and channel curvature in a curved channel. The radial baffles and channel curvature were responsible for multidirectional vortices and converging-diverging flow, resulting in enhanced mixing efficiency.<sup>33</sup> T and Y shaped micromixers were also proposed in the literature.<sup>34–37</sup> Wang *et al.* presented a case of the mixing of fluid streams in “Y” type microchannels, using cylindrical-shaped obstacles for enhancing the mixing performance. The significant effect of proper placement and position of obstacles was demonstrated at Reynolds numbers in the range from 0.5 to 60. The formation of vortex pairs in T shaped microchannels was argued as the reason for enhancement in the mixing performance.<sup>35</sup> Shih-Jeh *et al.*<sup>38</sup> designed a microchannel with cylindrical obstacles and observed tooth notches to improve the fluid mixing at Re values in the range 0.01–100. Yang *et al.*<sup>39</sup> proposed a three-dimensional Tesla structured micromixer to achieve efficient mixing for a range of Reynolds number from 0.1 to 100.

We present novel designs of passive microfluidic mixers and validate the mixing performance of these designs. Numerical simulations of various geometrical designs of microchannels such as U-shaped, fish-shaped, and spirals were performed. We also performed simulations of obstacle-laden and obstacle-less designs to study the effect of channel occlusion on micromixing. Larger-scale microchannel designs that incorporate microfabricated obstacles were fabricated and tested. The experimental results based on optimized channel designs indicate reasonable agreement in mixing performance when compared with numerical predictions. We utilized and optimized the micromixer design for on-chip imaging of serum calcium, which is a key biomarker for several pathological conditions. Although mixing in curved channel geometries is reported in the literature, the combined effect of channel-laden obstacles and channel curvature on the mixing performance is worthwhile to be explored, and the reported design modifications contribute to further enhancing the mixing efficiency. This argument forms the basis of the present work. In addition, the proposed micromixing designs are validated for biological applicability where direct colorimetric and confocal imaging of serum calcium is performed. This is worthwhile, considering the fact that calcium regulation is a vital factor in the case of many neurodegenerative diseases including Alzheimer’s disease.

## II. MATERIALS AND METHODS

### A. Numerical modeling

#### 1. Governing equations

The concentration field in the microchannels can be calculated by solving coupled field equations of mass and momentum transport. In the present study, flow modeling is performed by considering fluids as incompressible Newtonian liquids. The fluid flow model is described by the Navier–Stokes equation<sup>20</sup> and continuity equation, expressed as

$$\rho \frac{\partial U}{\partial t} + \rho(U \cdot \nabla)U = -\nabla p + \mu \nabla^2 U + F, \quad (1)$$

$$\nabla \cdot U = 0. \quad (2)$$

In the above equations,  $U$  represents the fluid velocity (m/s),  $\rho$  is the fluid density,  $p$  is pressure (Pa),  $\mu$  is the dynamic viscosity of the fluid, and  $F$  represents body forces per unit volume. The concentration field inside the microchannel can be represented by the convection–diffusion equation, which is expressed as

$$\frac{\partial c}{\partial t} + (U \cdot \nabla)c = D \nabla^2 c. \quad (3)$$

The boundary conditions (on the channel walls) for which the convection–diffusion equation is solved for the designed geometry are

$$-n \cdot N_i = 0, \quad N_i - D_i \nabla c_i + U c_i = 0. \quad (4)$$

In the above equations,  $n$  is the normal vector,  $N_i$  is the mass flux of the  $i$ th species,  $c$  represents the species concentration (mol/m<sup>3</sup>), and  $D$  is the diffusion coefficient of the species (m<sup>2</sup>/s). Equation (4) indicates that the mass transport perpendicular to the microchannel surface is considered to be zero, a fairly reasonable assumption considering non-porous channels. In the present study, a uniform concentration of species was assumed at the inlets of the channel. This means inlet conditions  $c = 1$  and  $c = 0$  were assumed for the two inlets of the microchannel, and the proximity to the condition  $c = 0.5$  was considered to be the case of ideal mixing. The initial species concentration in the microchannel was assumed to be zero. The designs studied in the present work were identified based on the idea of mixing enhancement due to secondary flow vortices resulting from the channel curvature and the presence of micro-obstacles (which results in flow splitting and recombination). Curved channel geometries can induce Dean vortices perpendicular to the direction of flow,<sup>40</sup> where a smaller radius of curvature results in higher values of Dean numbers. The Dean number can be defined as  $De = Re \sqrt{D_h/2R}$ , where  $D_h$  is the hydraulic diameter,  $R$  is the radius of curvature of the microchannel, and  $Re$  is the Reynolds number. The Dean number represents the ratio of centrifugal and inertial forces to viscous force.<sup>41</sup>

#### 2. Geometry and mesh optimization

The concentration field in the microchannels was numerically simulated using finite element software COMSOL 5.0. We performed a mesh independence study to confirm that numerical results are independent of the mesh number of elements (using sequences such as 1×, 2×, 4×, and 8× number of elements). The flow and concentration conditions at the channel inlets and boundaries

were assumed as described in Sec. II A 1. These tests were performed on spiral and obstacle-laden fish channel designs. The steady-state simulation results corresponding to the fish-shaped design and spiral-shaped design are included in Tables I and II, respectively. The simulation results corresponding to varying mesh sizes ( $1\times$ – $8\times$ ) are presented. We observed a negligible variation in the calculated values of the concentration field, beyond a mesh size of 18 000 elements (approximate). In addition, the oscillations in the concentration field (corresponding to  $1\times$  and  $2\times$  mesh density) calculated close to the entrance to the main channel was minimized beyond the mesh size of 18 000 elements. Hence, an optimized mesh size of nearly 18 000 triangular elements was used for performing all the simulations in the present study. We performed local refinement of the mesh close to boundaries that define the obstacles (in the case of the obstacle-laden design), smaller radius of curvatures (in the case of the spiral design), and regions of flow expansion. The mesh refinement was performed to track the larger gradients of the concentration field close to the abovementioned boundaries. The addition of numerical diffusion can occur in numerical simulations due to the discretization of convective terms for determining the concentration distribution. The degree of numerical diffusion can be limited, utilizing higher-order discretization.<sup>42</sup> In the present simulations, higher-order discretization was used to minimize the degree of artificial diffusion.




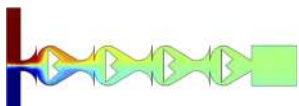

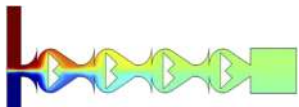

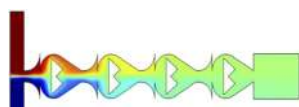
## B. Experimental setup

Following numerical simulations, we fabricated optimized designs—spiral-shaped and fish-shaped (obstacle-laden) channel structures. Microfluidic designs were prepared by utilizing standard

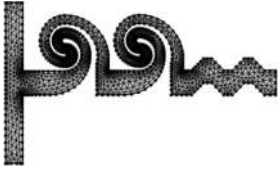

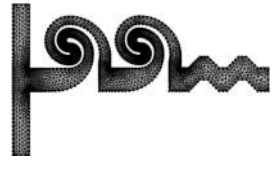





soft-lithography techniques. Primarily, the silicon wafer was cleaned and dehydrated. The cleaned wafer was coated with negative photoresist SU-8 2050 at 3000 RPM to get the  $50\ \mu\text{m}$  thickness by using a spin coater. Then, the SU-8 coated wafer was soft-baked on a hotplate at  $65^\circ\text{C}$  for 3 min and  $95^\circ\text{C}$  for 6 min. Furthermore, the processed wafer was exposed inside the UV LED exposure system (UV-KUB) to pattern the SU8 mold. The post-bake was performed at  $65^\circ\text{C}$  for 2 min and  $95^\circ\text{C}$  for 6 min, and the master mold was obtained after the development process. Once the mold was prepared, PDMS (Sylgard 184 from Dow Corning and curing agent) with the proportion of 10:1 ratio was poured onto the SU-8 master mold after degassing under a vacuum oven. Curing was performed for 60 min at  $80^\circ\text{C}$  by a thermal vacuum oven. PDMS replicas were peeled off from the SU-8 master mold and bonded with glass slides after plasma treatment. Hill-shaped obstacles (Table I) in the microfluidic channels were made of SU8, and the corresponding portions in mask designs were light exposed parts of SU8 molded as a pillar. The schematic of the spiral design is presented in Table II.

Micromixing experiments were performed using a multiple syringe pump. We used red and yellow dye solutions to test the mixing performance of the fabricated microfluidic designs. Images of the microchannel cross sections [along the length of the microchannel, marked as c1–c5 in Figs. 1(b), 2(b) and 5(a–ii)] were captured using a high-quality digital camera. These experiments were performed using spiral-shaped and obstacle-laden fish-shaped channels. The image color intensity was calculated using an image processing software (ImageJ). The resulting values (experimental and numerical) are normalized by using the formula  $\frac{c - c_{min}}{c_{max} - c_{min}}$  (where  $c$  represents the dye concentration).

TABLE I. Mesh independency test using the fish-shaped channel design.

Number of elements	Meshed channel	Simulation results
4 623( $1\times$ )		
9 330( $\sim 2\times$ )		
18 529( $\sim 4\times$ )		
36 984( $\sim 8\times$ )		

**TABLE II.** Mesh independency test using the spiral-shaped channel design.

Number of elements	Meshed channel	Simulation results
3 293(1×)		
6 582(~2×)		
13 283(~4×)		
26 331(~8×)		

### III. RESULTS AND DISCUSSION

#### A. 2D simulations

##### 1. Case 1: Obstacle-less microchannels

The geometrical features of obstacle-less designs are presented in Table III. Designs involving converging–diverging boundaries are presented. The geometric dimensions of these channel designs are indicated in Table III. In the case of corner-shaped and U-shaped designs, the width of the channel inlet ( $w_1$ ) was  $60\ \mu\text{m}$ , the total axial length of the channel from the inlet to the outlet ( $l_2$ ) was  $1260\ \mu\text{m}$ , the maximum width of the mixing chamber ( $w_2$ ) was  $250\ \mu\text{m}$ , and the length of one mixing chamber ( $l_1$ ) was  $180\ \mu\text{m}$ . The mixing chamber aspect ratio ( $w_2/l_1$ ) in the case of corner-shaped and U-shaped designs was chosen higher than 1 in order to generate designs that allow rapid flow convergence and to generate stronger secondary flow vortices in the chambers. However, this restriction was not imposed on fish-shaped designs as these designs contained sharp wedges in the proximity of the converging–diverging sections of the mixing chambers. In the case of fish-shaped designs, all other geometric parameters ( $w_1$ ,  $l_1$ ,  $l_2$ ) remained the same as in the case of the other two converging–diverging designs.

Channel geometries include converging–diverging boundaries, present at periodic intervals along the channel length. These designs increase the length of fluid contact in the microchambers.<sup>43</sup> In addition, these convergence–divergence pathways form symmetric vortices at the throat of each sub-channels, increasing local

convective transport in the microchambers. Numerical simulations indicate that the mixing length increases with an increase in channel inlet velocity (flow Reynolds number), and concurrently, the mixing time reduces. However, this phenomenon occurs within a particular range of velocity and is dependent on the channel geometry. Figure 1(a) presents the simulation results corresponding to various types of obstacle-less channel designs.

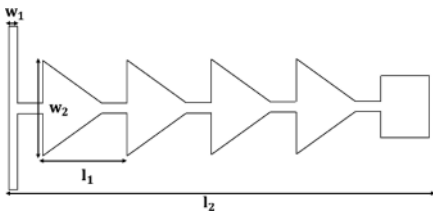
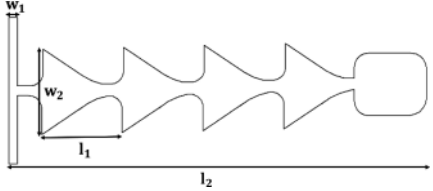
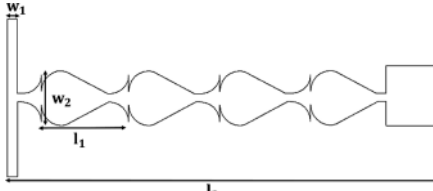
Figure 1(b) demonstrates the difference between corner-, U-, and fish-shaped designs, in terms of the peak concentration difference ( $\zeta = C_{max} - C_{min}$ ) corresponding to different chamber positions [indicated as c1–c5 in Fig. 1(b)] along the channel.  $\zeta$  represents the difference between the steady-state values of the maximum ( $C_{max}$ ) and minimum ( $C_{min}$ ) concentration corresponding to different positions along the channel. It is observed that the concentration difference ( $\zeta$ ) is almost close to zero at the outlet, indicating adequate mixing in the channel. It can be noted that the  $\zeta$  value in the case of the fish-shaped channel design is significantly lesser, even with an aspect ratio ( $w_2/l_1$ ) less than 1. Therefore, the fish-shaped design can be argued to be better compared to other designs. Channel curvatures and a larger number of turning points compared to corner- and U-shaped channels result in better mixing performance in the case of a fish-shaped design.

##### 2. Case 2: Obstacle-laden microchannels

In an effort to study the effect of obstacles on micromixing performance, we simulated obstacle-laden channel designs by using similar boundary and initial conditions, as described in Sec. II A 1.



TABLE III. Schematics of obstacle-less microfluidic mixer designs.

Schematics of microchannel designs	$w_1$	$l_1$	$w_2$	$l_2$
 <p>Corner-shaped design</p>	Width of the inlet	Length of one mixing chamber	Maximum width of the mixing chamber	Total axial length of the channel
 <p>U-shaped design</p>	Width of the inlet	Length of one mixing chamber	Maximum width of the mixing chamber	Total axial length of the channel
 <p>Fish-shaped design</p>	Width of the inlet	Length of one mixing chamber	Maximum width of the mixing chamber	Total axial length of the channel

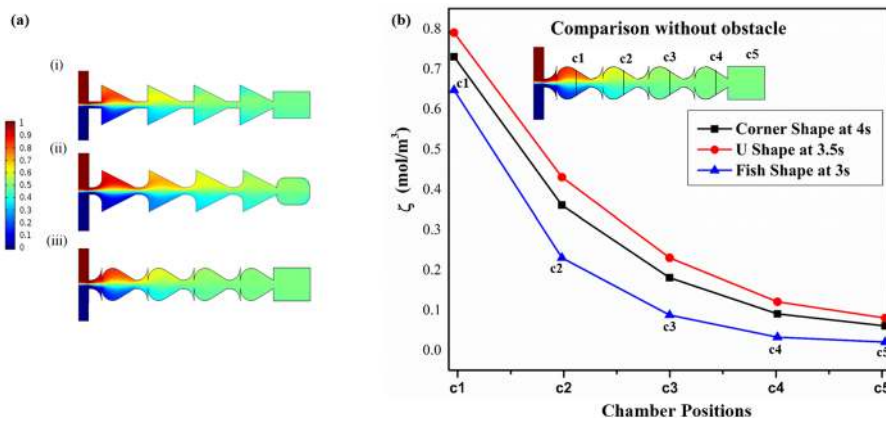
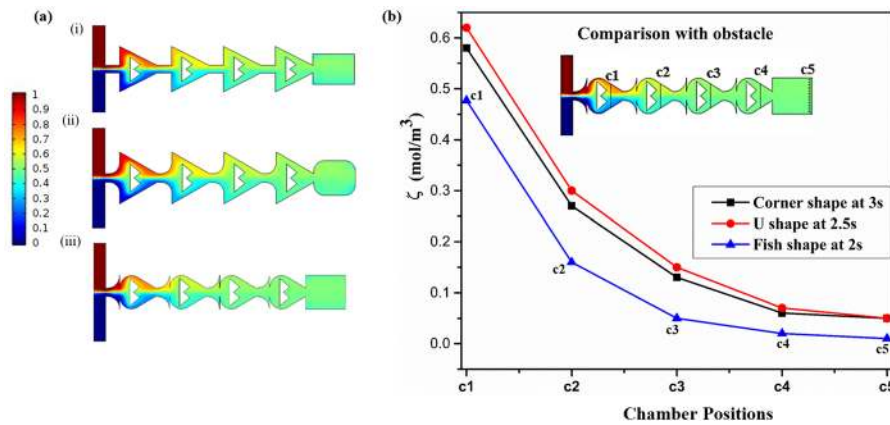


FIG. 1. (a) Simulation results (steady-state concentration field) of obstacle-less channel designs corresponding to an inlet velocity of  $12 \times 10^{-4}$  m/s [(a-i)–(a-iii)]. (b) Variation in the concentration difference ( $\zeta$ ) corresponding to chamber positions (c1–c5) from the inlet. The corresponding distances from the inlet are  $190 \mu\text{m}$ ,  $440 \mu\text{m}$ ,  $690 \mu\text{m}$ ,  $940 \mu\text{m}$ , and  $1190 \mu\text{m}$ .

The simulation results are presented in Fig. 2(a). We observed that the mixing performance of the microfluidic designs is improved by the introduction of obstacles in the microchannels, and mixing time is reduced as well, as summarized in Table IV.

The obstacles disrupt the fluid flow and reduce the diffusion path. The direction of flow, from one fluid to another, is altered due to the disruption of the velocity flow field. Therefore, obstacles can generate additional secondary flow vortices in the channels, improving the mixing performance.  $\zeta$  values calculated in the case of

multiple obstacle-laden designs corresponding to various positions (c1–c5) along the channel length are plotted as presented in Fig. 2(b). The  $\zeta$  value for a particular chamber position is reduced in the case of obstacle-laden designs, indicating the effect of channel occlusion on micromixing. Figure 3 presents the comparison between obstacle-less and obstacle-laden designs, where the time evolution of concentration profiles at the outlet of the fish-shaped channel is presented. It is clear from Fig. 3 that the concentration profile becomes flat at  $c = 0.5$  at a faster pace compared to obstacle-less designs. Besides,



**FIG. 2.** (a) Simulation results (steady-state concentration field) of obstacle-laden channel designs corresponding to an inlet velocity of  $12 \times 10^{-4}$  m/s [(a-i)–(a-iii)]. (b) Variation in the concentration difference ( $\zeta$ ) corresponding to chamber positions (c1–c5) from the inlet. The corresponding distances from the inlet are  $190 \mu\text{m}$ ,  $440 \mu\text{m}$ ,  $690 \mu\text{m}$ ,  $940 \mu\text{m}$ , and  $1190 \mu\text{m}$ .

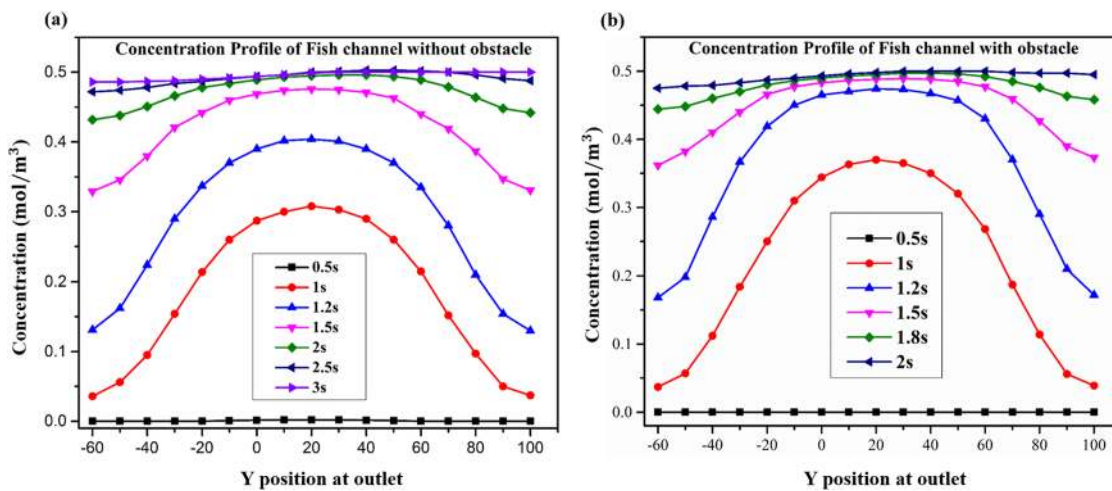
**TABLE IV.** Mixing time of various microfluidic designs corresponding to an inlet velocity of  $12 \times 10^{-4}$  m/s.

	Corner-shaped (s)	U-shaped (s)	Fish-shaped (s)
Obstacle-less designs	4	3.5	3
Obstacle-laden design	3	2.5	1.9

the performance of the fish-shaped design is observed to be consistently better compared to other designs, which is understandable as per the previous discussion. The integration of obstacles enhances the mixing efficiency as observed by lower  $\zeta$  values.

The simulation results presented in Fig. 2 correspond to the inlet velocity of  $12 \times 10^{-4}$  m/s. The variation in the local Reynolds number for the fish-shaped channel design is presented in Fig. 4. The local Reynolds number in the obstacle-less fish-shaped

channel is calculated as 0.142, based on the center-width of the channel [Fig. 4(a)]. The local Reynolds number in the obstacle-laden fish channel is calculated based on varying hydraulic diameter closer to a positioned obstacle, as presented in Fig. 4(b). A significant variation in local Re can be observed near narrowed cross sections closer to obstacles. The introduction of micro-obstacles in the fish-shaped channel results in a twofold increase in local Re close to the sharp edges of the obstacle close to the channel boundary. This results in enhanced local convective transport, consequently resulting in increased efficiency of mixing. The increase in the efficiency of mixing in the case of obstacle-laden corner- and U-shaped designs can be explained along similar lines as identical obstacles are introduced in these designs as well. The results from simulations of obstacle-laden designs also confirm the observation that the fish-shaped design performs better compared to the other two designs. Therefore, in addition to the obstacle geometry, the outer geometry of the microchamber is also observed to play an important role in micromixing.



**FIG. 3.** Evolution of the concentration profile at the channel outlet in the case of the (a) obstacle-less fish-shaped channel and (b) obstacle-laden fish-shaped channel.

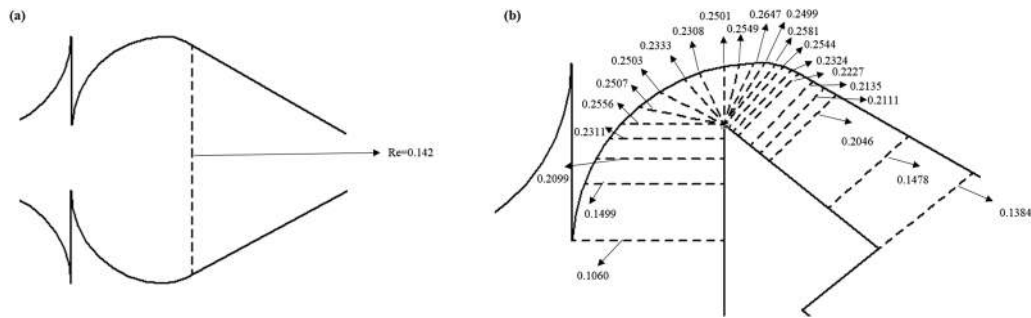


FIG. 4. Local Reynolds number in (a) obstacle-less fish-shaped channel and (b) obstacle-laden fish-shaped channel.

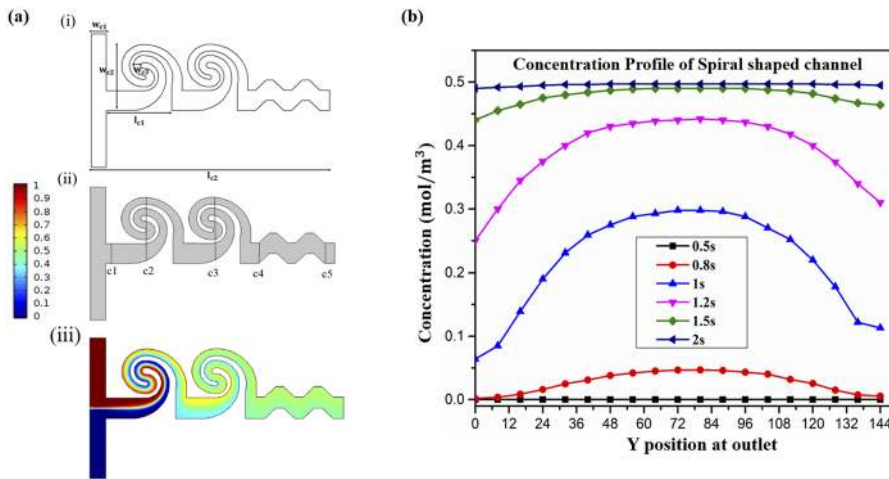


FIG. 5. (a) (i) Schematics of the spiral microchannel design, (ii) schematic of positions along the channel length, and (iii) simulation results (steady-state concentration field) of spiral designs corresponding to an inlet velocity of  $22 \times 10^{-4}$  m/s. (b) Time evolution of the concentration profile at the spiral channel outlet (C5).

### 3. Case 3: Spiral-shaped microchannels

We studied the mixing performance of two-stage spiral channel designs. The schematic of the spiral designs is presented in Fig. 5(a). The inlet width of the channel ( $w_{c1}$ ) is  $100 \mu\text{m}$ , the total axial length from the inlet to outlet ( $l_{c2}$ ) is  $1500 \mu\text{m}$ , the width of the spiral curve ( $w_{c3}$ ) is  $50 \mu\text{m}$ , the length of one mixing chamber ( $l_{c1}$ ) is  $440 \mu\text{m}$ , and the maximum width of the spiral chamber ( $w_{c2}$ ) is  $470 \mu\text{m}$ , as illustrated in Fig. 5(a-i).

The time evolution of the concentration profile at the outlet of the spiral design is presented in Fig. 5(b). The mixing performance of the spiral channel microfluidic design can be attributed to secondary vortices. Secondary Dean flows play a significant role in curved channel micromixing. The magnitude of counter-rotating dean flows increases with an increase in the Dean number. The Dean number corresponding to various curvature values of spiral design is presented in Fig. 6. The strength of the secondary flow is the highest at the inner curvature of the spiral design where  $De = 0.105$ . The primary reason for mixing is the increase in the fluid acceleration as fluid streams travel from the outer region to the inner region of the curved channel route, where the radius of curvature is small.<sup>44</sup>

Figure 7 depicts a comparison between the obstacle-laden fish-shaped design and the spiral-shaped design. The mixing times for

a range of Reynolds numbers are presented. We observed that as the Reynolds number increases, the mixing time decreases in a particular range of Reynolds numbers, which is in agreement with the reported literature.<sup>21-24,44</sup> Furthermore, an interesting contradiction is observed when comparing the mixing performance of these two

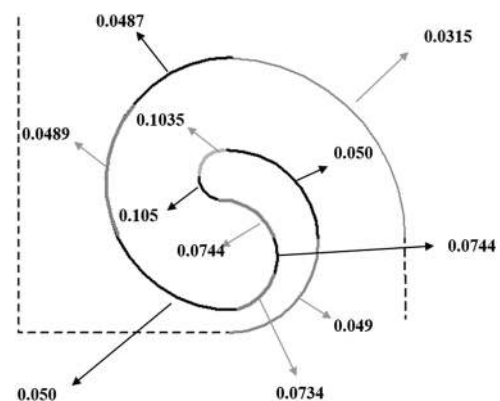


FIG. 6. Dean number of the spiral-shaped geometry along with the spiral contour corresponding to a Reynolds number value of 0.12.



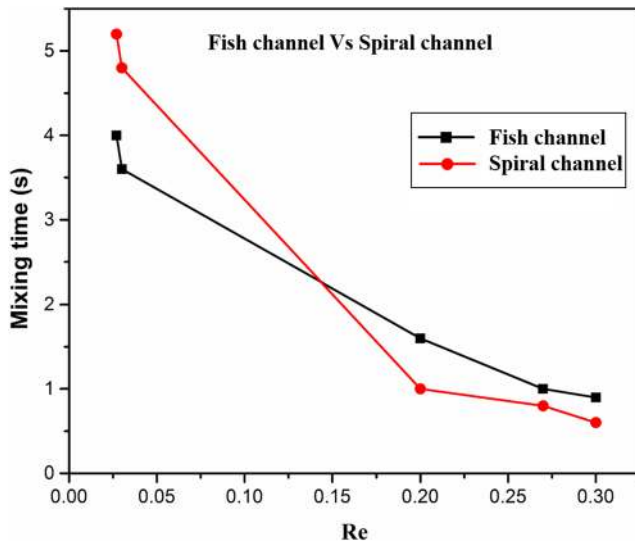


FIG. 7. Comparison between obstacle-laden fish-shaped and spiral-shaped channel designs corresponding to inlet flow Reynolds number values of 0.027, 0.03, 0.2, 0.27, and 0.3.

designs. The mixing time in the case of the spiral-shaped design is lesser at a high Reynolds number. However, we observed the reverse case at a low Reynolds number. At a low Reynolds number, the mixing performance is higher in the obstacle-laden fish-shaped channels in comparison with spiral designs. This effect can be attributed to the combined effect of obstacles and converging-diverging boundaries that result in improved mixing at lower Re values. The efficiency of mixing in the case of spiral design is mostly dependent on secondary vortex flows. It can be interpreted that at low Reynolds numbers, the mixing performance of spiral channel designs is limited on account of the limited strength of secondary vortices. The effect of obstacles on the mixing performance is observed to be less pronounced beyond a critical value of the Reynolds number. Hence, it can be concluded that the obstacle-laden fish-shaped design is in general efficient at lower flow velocities, an experimental requirement in the case of many on-chip cell culture designs.<sup>45</sup> However, it should be emphasized that the overall dimensions of the channel are important as well, as we have compared two different types of mixing designs. The mixing efficiency of these designs can be further improved by incorporating multiple obstacles of different geometries or by increasing the number of spiral sections. The channel geometry should be selected as per the practical requirement of flow conditions needed, as well as by analyzing the

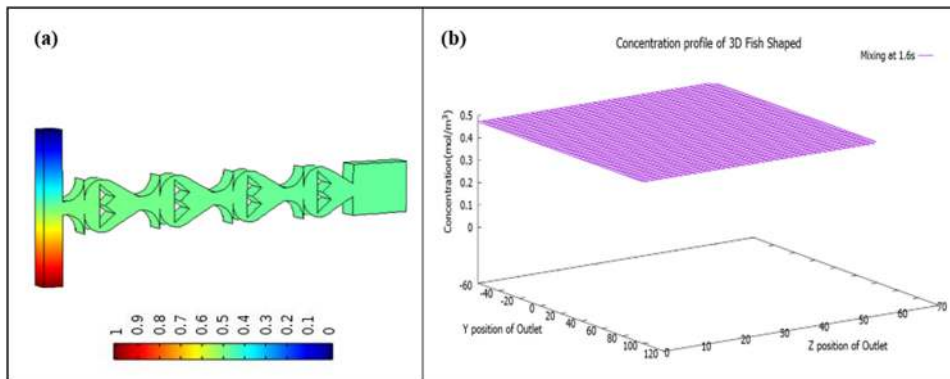


FIG. 8. (a) Simulation results of the obstacle-laden fish-shaped channel and (b) steady-state concentration profile of the 3D fish-shaped channel at the extreme outlet of the channel. Inlet velocity =  $12 \times 10^{-4}$  m/s.

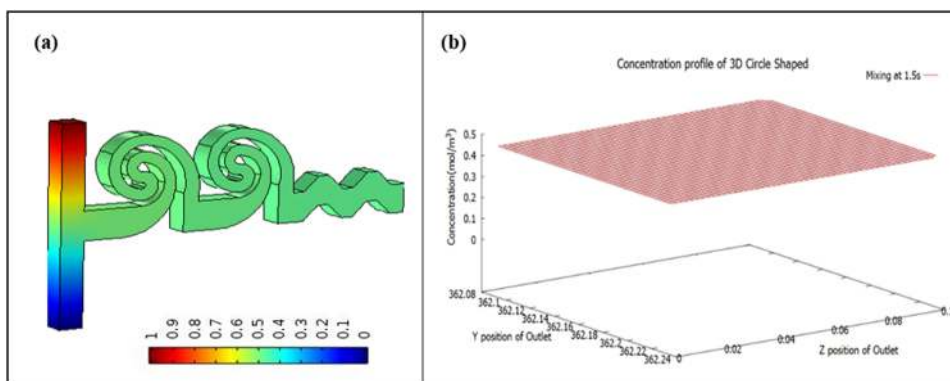


FIG. 9. (a) Simulation results of the 3D spiral-shaped channel and (b) steady-state concentration profile of the spiral-shaped channel at the extreme outlet of the channel. Inlet velocity =  $22 \times 10^{-4}$  m/s.

channel performance at the required range of inlet velocity/Reynolds numbers.

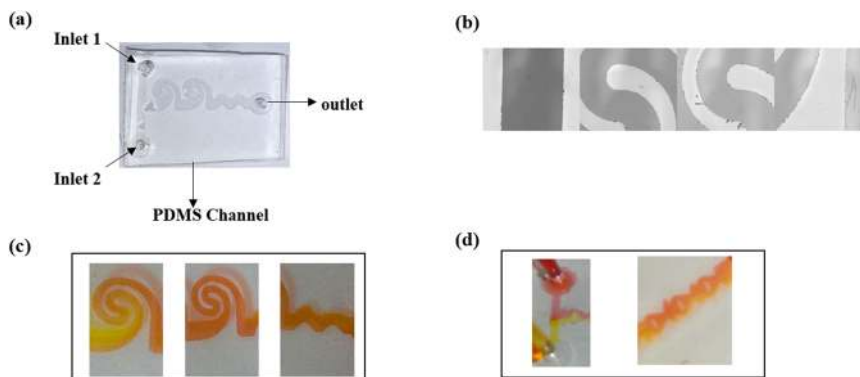
### B. 3D simulations

We performed simulations of 3D designs of obstacle-laden fish and spiral geometry designs where the channel height assumed was  $50\ \mu\text{m}$ . These simulations were performed with an identical set of inlet, initial, and boundary conditions. Four node tetrahedral elements were used for meshing the 3D domain for simulations, and selective mesh refinement close to critical boundaries was performed, as indicated in Sec. II A 2. 3D simulation results of a fish-shaped design incorporating hill type obstacles are presented in Fig. 8(a). The steady state concentration profile at the extreme outlet of the channel is depicted in Fig. 8(b). The flat concentration profile at the channel outlet corresponding to  $c = 0.5\ (\text{mol}/\text{m}^3)$  indicates

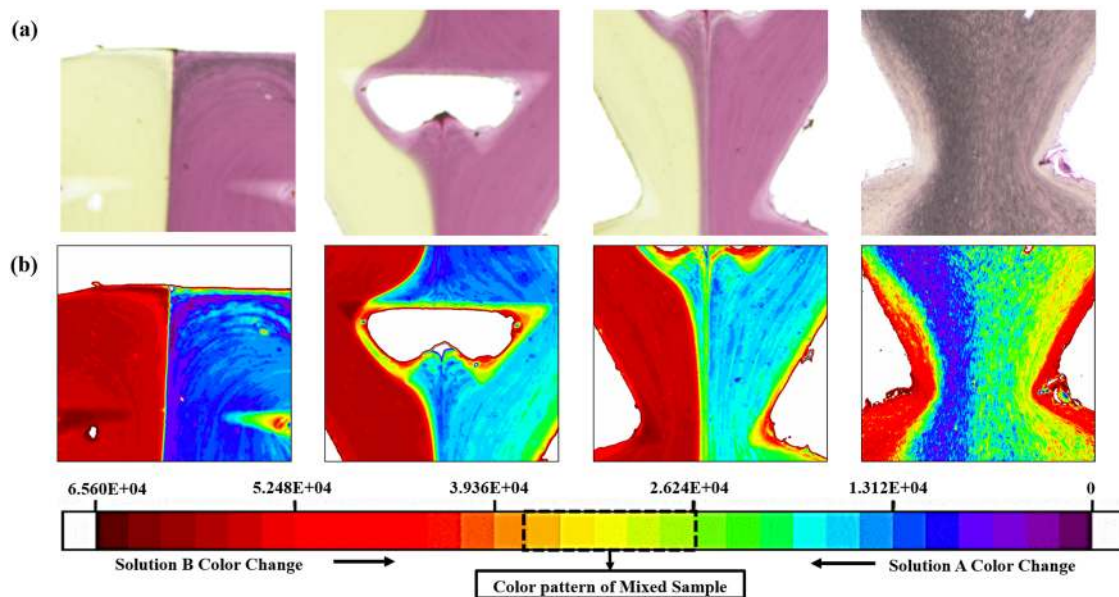
uniform mixing. It can be noted that the difference between the mixing time of 2D and 3D fish-shaped channel designs is 0.3 s (1.9 s for the case of 2D designs and 1.6 s for the case of 3D designs). A similar trend is observed for the case of spiral channel designs (Fig. 9) where the difference in mixing time between 2D and 3D designs is 0.3 s. However, it is observed that the 3D channel results indicate effective mixing from cross sections much closer to the entrance, as compared to 2D. This means the value of the concentration difference ( $\zeta$ ) is closer to zero from sections c1 (marked along the channel in Figs. 2 and 5) onward.

### IV. MICROMIXING EXPERIMENTS USING SPIRAL AND OBSTACLE-LADEN FISH-SHAPED CHANNELS

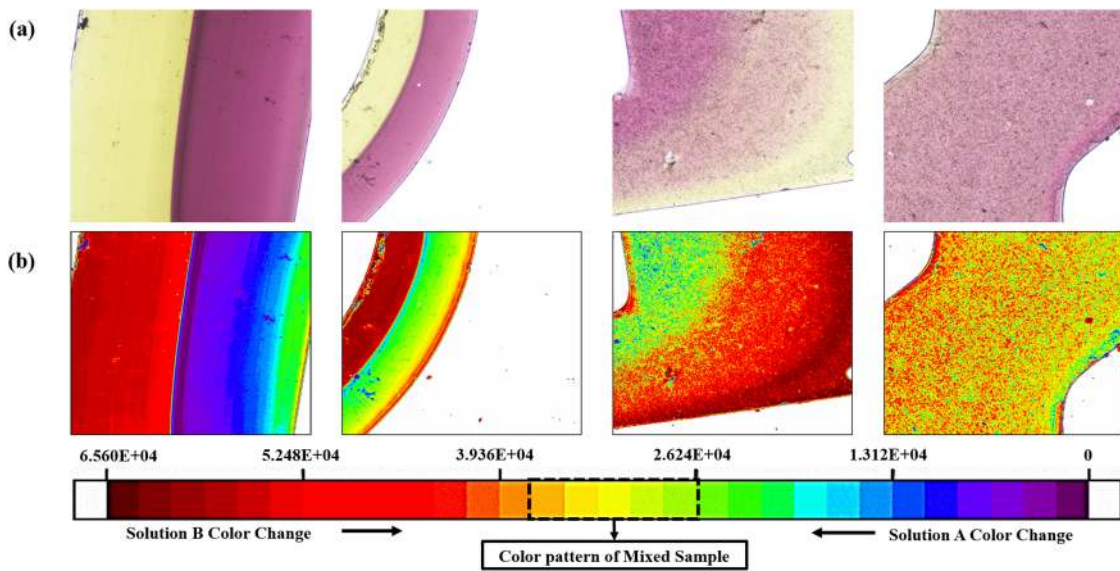
In order to validate the mixing behavior of the simulated microchannel designs, we performed experiments using fabricated



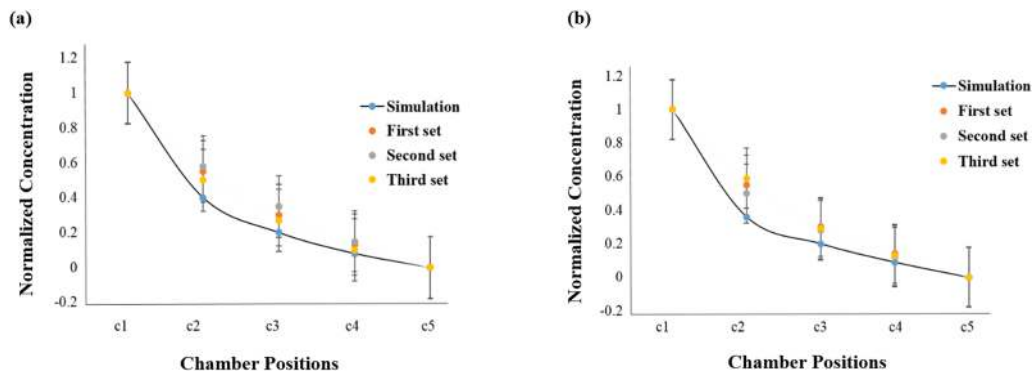
**FIG. 10.** (a) Fabricated micromixer. (b) Microscopic grayscale image of dye-DI water mixing in the microchannel. (c) Micromixing in spiral sections from the inlet to the outlet, corresponding to an inlet velocity of  $22 \times 10^{-4}\ \text{m/s}$ . (d) Micromixing in the obstacle-laden fish-shaped channel, corresponding to an inlet velocity of  $12 \times 10^{-4}\ \text{m/s}$ .



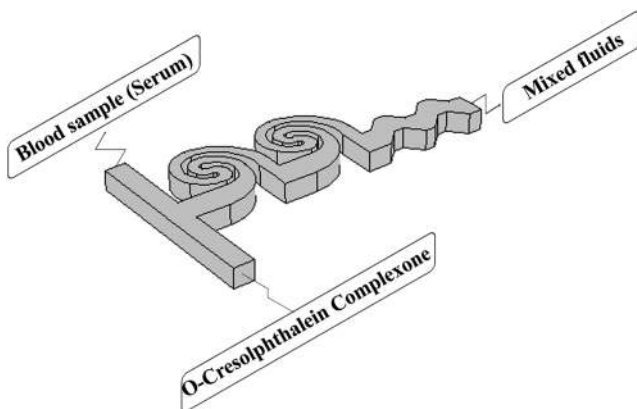
**FIG. 11.** Digital color images of yellow and pink dyes entering the obstacle-laden fish-shaped channel and mixing pattern in various sections: (a) images of enlarged ROIs obtained from the various region of interest and (b) the corresponding contours to visualize the evolution of the yellow-green interface in the proposed channel.



**FIG. 12.** Digital color images of yellow and pink dyes entering the spiral channel and mixing pattern in various sections: (a) images of enlarged ROIs obtained from the various region of interest and (b) the corresponding contours to visualize the evolution of the yellow–green interface in the proposed channel.

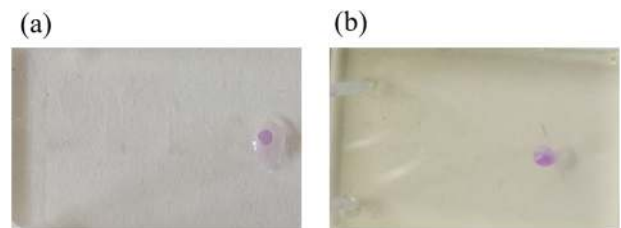


**FIG. 13.** Normalized concentration values from simulation and experiments, corresponding to various positions of the microfluidic mixing chamber: (a) spiral-shaped design and (b) fish-shaped design.

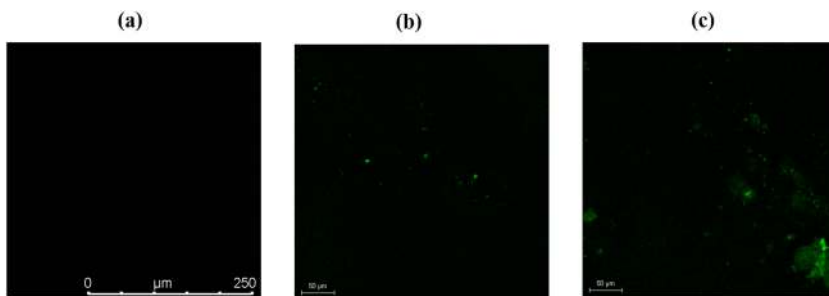


**FIG. 14.** Flow diagram of the osteoporosis experiment.

designs of spiral-shaped and obstacle-laden fish-shaped channels. Figure 10 shows the results of color dye mixing in the microchannel designs. In the case of both designs, it can be observed that efficient mixing is achieved closer to the channel outlet. Furthermore, to



**FIG. 15.** On-chip calcium detection using the spiral micromixing design: (a) female sample and (b) male sample.



**FIG. 16.** Confocal imaging of serum calcium by using calcium-sensitive fluoro-4 dye. (a) Channel inlet that does not show fluorescence. (b) Channel center where the fluids are getting mixed. (c) Channel outlet where visible dye fluorescence is detected, which indicates the presence of calcium in the serum sample.

visualize the mixing, the contour images from mixing experiments were obtained corresponding to various regions of interest (ROIs) along the path length of both channels, and the resulting contours are depicted in Figs. 11 and 12. The results visibly indicate the mixing pattern inside both channels. It can be observed from Fig. 11 that the flow pattern is perturbed by the presence of the obstacles, resulting in efficient flow mixing in the channel. Similarly, the ROI along the path length of the spiral channel (Fig. 12) indicates patterns corresponding to efficient mixing.

We performed a quantitative comparison of simulation results with micromixing experimental data. Experimental validation of obstacle-laden fish- and spiral-shaped designs is presented in Fig. 13. Normalized concentration (defined in Sec. II B) values corresponding to different positions along the channel length are plotted. Experimental replication is represented by the first, second, and third sets in Fig. 13. No significant difference was observed between numerical and experimental results, specifically when results corresponding to the channel outlet are compared. The minor discrepancy between theory and experiment could be attributed to flow development effects and fluid properties.

## V. MICROMIXING EXPERIMENTS FOR SERUM CALCIUM DETECTION

We evaluated the performance of the optimized spiral mixing design by performing biological experiments for serum calcium detection. The preliminary recommended tests for the identification of a prevalent bone disorder—osteoporosis—are serum calcium and serum Alkaline Phosphatase (ALP).<sup>46</sup> The principle of the on-chip experiment is based on the fact that calcium in the alkaline solution reacts with O-Cresolphthalein Complexone (O-CPC) to form a purple complex. In order to perform this test, we used real blood samples and centrifuged the samples to separate the serum at 2500 RPM for 20 minutes. Furthermore, blood serum and o-cresolphthalein complexone were injected into the two inlets as depicted in the flow diagram (Fig. 14). The O-CPC reagent and sample (serum) would flow through the spiral microfluidic channel, and the channel outlet is imaged. The result of efficient mixing is a purple complex, as presented in Fig. 15. The intensity of the color formed is directly proportional to the amount of calcium present in the sample.

The color intensity obtained in our design was compared with the pre-calibrated standard curve to quantify the levels of analyte in blood. The serum calcium level in our tested device was 9 mg/dl (female) and 9.5 mg/dl (male), which is well within the normal range. Furthermore, confocal images from the channel inlet to the

outlet are depicted in Fig. 16. The inlet of the spiral microfluidic channel does not show visible fluorescence because of sample mixing close to the channel entrance. Green fluorescence is observed close to the center and outlet of the microfluidic channel. The green color in the confocal images indicates the presence of calcium in the serum sample, thereby confirming the efficient mixing of blood serum and o-cresolphthalein complexone inside the channel.

## VI. CONCLUSION

The present study focuses on the evaluation of different types of microfluidic mixing designs. We studied the effect of obstacles on micromixing by performing numerical simulations and experiments. It was observed that the presence of channel-laden obstacles significantly impacts the mixing performance. Besides, the geometry of the obstacle was observed to play a significant role, as an enhancement in local values of Reynolds numbers up to twice the average value was observed in the vicinity of sharper obstacles. Obstacle-laden fish-shaped designs and spiral-shaped channel designs offer better mixing performance owing to secondary flows, produced as a result of the channel curvature and the presence of obstacles. We observed interesting crossover in the mixing performance dependent on the flow Reynolds number when comparing the obstacle-laden fish and spiral channel designs. Numerical simulations indicated mixing time less than 2 s in the case of optimized designs.<sup>47</sup> This is worthwhile in designing on-chip cell assays, considering the cell-drug interaction timescales. Furthermore, experimental validation using optimized designs indicates reasonably good agreement with model predictions. The mixing performance could be improved further using a channel aspect ratio (maximum chamber width to depth ratio, which is 5 in the present study) closer to 1. An optimized spiral mixing design was utilized for on-chip calcium detection from blood serum. Confocal microscopic experiments were performed, where serum calcium was imaged at different locations along the length of the spiral microfluidic design. The confocal results indicate the presence of calcium in blood serum close to the channel outlet. This highlights the utility of the proposed designs for on-chip bioimaging applications such as monitoring serum calcium levels in Alzheimer's disease. The proposed designs could be utilized as micromixing platforms for cell-based biosensing and immunoassays.

## ACKNOWLEDGMENTS

The authors are thankful to the Ministry of Education (MoE), India, for financial support.



## DATA AVAILABILITY

The data that support the findings of this study are available within the article.

## REFERENCES

- <sup>1</sup>N. S. Lynn, Jr. and J. Homola, "Biosensor enhancement using grooved micromixers: Part I numerical studies," *Anal. Chem.* **87**(11), 5516–5523 (2015).
- <sup>2</sup>M. Madadelahi, E. Ghazimirsaeed, and A. Shamloo, "Design and fabrication of a two-phase diamond nanoparticle aided fast PCR device," *Anal. Chim. Acta* **1068**, 28–40 (2019).
- <sup>3</sup>P. Cui and S. Wang, "Application of microfluidic chip technology in pharmaceutical analysis," *J. Pharm. Anal.* **9**(4), 238–247 (2019).
- <sup>4</sup>V. Hessel, H. Löwe, and F. Schönfeld, "Micromixers: A review on passive and active mixing principles," *Chem. Eng. Sci.* **60**, 2479–2501 (2005).
- <sup>5</sup>N.-T. Nguyen and Z. Wu, "Micromixers: A review," *J. Micromech. Microeng.* **15**, R1 (2005).
- <sup>6</sup>C.-Y. Lee, C.-L. Chang, Y.-N. Wang, and L.-M. Fu, "Microfluidic mixing: A review," *Int. J. Mol. Sci.* **12**, 3263–3287 (2011).
- <sup>7</sup>K. Ward and Z. H. Fan, "Mixing in microfluidic devices and enhancement methods," *J. Micromech. Microeng.* **25**, 094001 (2015).
- <sup>8</sup>C.-Y. Lee, W.-T. Wang, C.-C. Liu, and L.-M. Fu, "Passive mixers in microfluidic systems: A review," *Chem. Eng. J.* **288**, 146–160 (2016).
- <sup>9</sup>J.-H. Tsai and L. Lin, "Active microfluidic mixer and gas bubble filter driven by thermal bubble micropump," *Sens. Actuators, A: Phys.* **97–98**, 665–671 (2002).
- <sup>10</sup>C. Westerhausen, L. G. Schnitzler, D. Wendel, R. Krzysztosń, U. Lächelt, E. Wagner, J. O. Rädler, and A. Wixforth, "Controllable acoustic mixing of fluids in microchannels for the fabrication of therapeutic nanoparticles," *Micromachines* **7**, 150 (2016).
- <sup>11</sup>H. H. Bau, J. Zhong, and M. Yi, "A minute magneto hydrodynamic (MHD) mixer," *Sens. Actuators, B: Chem.* **79**, 207–215 (2001).
- <sup>12</sup>S. C. Jacobson, T. E. McKnight, and J. M. Ramsey, "Microfluidic devices for electrokinetically driven parallel and serial mixing," *Anal. Chem.* **71**, 4455–4459 (1999).
- <sup>13</sup>E. M. Purcell, "Life at low Reynolds number," *Am. J. Phys.* **45**, 3–11 (1977).
- <sup>14</sup>A. L. Paguirigan and D. J. Beebe, "Microfluidics meet cell biology: Bridging the gap by validation and application of microscale techniques for cell biological assays," *BioEssays* **30**, 811 (2008).
- <sup>15</sup>H. Wang, P. Iovenitti, E. Harvey, and S. Masood, "Numerical investigation of mixing in microchannels with patterned grooves," *J. Micromech. Microeng.* **13**, 801 (2003).
- <sup>16</sup>J. Happel and H. Brenner, *Low Reynolds Number Hydrodynamics* (Prentice-Hall, 1965).
- <sup>17</sup>K. Benz, K.-P. Jäckel, K.-J. Regenauer, J. Schiewe, K. Drese, W. Ehrfeld, V. Hessel, and H. Löwe, "Utilization of micromixers for extraction processes," *Chem. Eng. Tech.* **24**, 11–17 (2001).
- <sup>18</sup>R. H. Liu, M. Ward, J. Bonanno, D. Ganser, M. Athavale, and P. Grodzinski, "Plastic in-line chaotic micromixer for biological applications," *Micro Total Anal. Syst.* 163–164 (2001).
- <sup>19</sup>C.-C. Hong, J.-W. Choi, and C. H. Ahn, "A novel in-plane passive microfluidic mixer with modified tesla structures," *Lab Chip* **4**, 109–113 (2004).
- <sup>20</sup>T. Zhou, Y. Xu, Z. Liu, and S. W. Joo, "An enhanced one-layer passive microfluidic mixer with an optimized lateral structure with the dean effect," *ASME J. Fluids Eng.* **137**, 090112 (2015).
- <sup>21</sup>V. Mengeaud, J. Josserand, and H. H. Girault, "Mixing processes in a zigzag microchannel: Finite element simulations and optical study," *Anal. Chem.* **74**, 4279–4286 (2002).
- <sup>22</sup>Y.-C. Chung, Y.-L. Hsu, C.-P. Jen, M.-C. Lu, and Y.-C. Lin, "Design of passive mixers utilizing microfluidic self-circulation in the mixing chamber," *Lab Chip* **4**, 70–77 (2004).
- <sup>23</sup>C.-H. Lin, C.-H. Tsai, and L.-M. Fu, "A rapid three-dimensional vortex micromixer utilizing self-rotation effects under low Reynolds number conditions," *J. Micromech. Microeng.* **15**, 935–943 (2005).
- <sup>24</sup>S. Hossain, M. A. Ansari, and K.-Y. Kim, "Evaluation of the mixing performance of three passive micromixers," *Chem. Eng. J.* **150**, 492–501 (2009).
- <sup>25</sup>W. Buchegger, C. Wagner, B. Lendl, M. Kraft, and M. J. Vellekoop, "A highly uniform lamination micromixer with wedge shaped inlet channels for time resolved infrared spectroscopy," *Microfluidics Nanofluidics* **10**, 889–897 (2011).
- <sup>26</sup>D. Gobby, P. Angeli, and A. Gavrilidis, "Mixing characteristics of T-type microfluidic mixers," *J. Micromech. Microeng.* **11**, 126–132 (2001).
- <sup>27</sup>A. D. Stroock, S. K. W. Dertinger, A. Ajdari, I. Mezic, H. A. Stone, and G. M. Whitesides, "Chaotic mixer for microchannels," *Science* **295**, 647–654 (2002).
- <sup>28</sup>B. He, B. J. Burke, X. Zhang, R. Zhang, and F. E. Regnier, "A picoliter-volume mixer for microfluidic analytical systems," *Anal. Chem.* **73**, 1942–1947 (2001).
- <sup>29</sup>R. H. Liu, M. A. Stremler, K. V. Sharp, M. G. Olsen, J. G. Santiago, R. J. Adrian, H. Aref, and D. J. Beebe, "Passive mixing in a three-dimensional serpentine microchannel," *J. Microelectromech. Syst.* **9**, 190–197 (2000).
- <sup>30</sup>S. H. Wong, M. C. L. Ward, and C. W. Wharton, "Micro T-mixer as a rapid mixing micromixer," *Sens. Actuators, B: Chem.* **100**, 359–379 (2004).
- <sup>31</sup>L. Li, "Design of micromixer and microfluidic control system," Ph.D. thesis, Florida Atlantic University, Boca Raton, FL, USA, 2013.
- <sup>32</sup>C. Y. Lee, C. F. Lin, M. F. Hung, R. H. Ma, C. H. Tsai, C. H. Lin, and L. M. Fu, "Experimental and numerical investigation into mixing efficiency of micromixers with different geometric barriers," *Mater. Sci. Forum* **505–507**, 391–396 (2006).
- <sup>33</sup>R.-T. Tsai and C.-Y. Wu, "An efficient micromixer based on multidirectional vortices due to baffles and channel curvature," *Biomicrofluidics* **5**, 014103 (2011).
- <sup>34</sup>W. Wang, S. Zhao, T. Shao, Y. Jin, and Y. Cheng, "Visualization of micro-scale mixing in miscible liquids using  $\mu$ -LIF technique and drug nano-particle preparation in T-shaped microchannels," *Chem. Eng. J.* **192**, 252–261 (2012).
- <sup>35</sup>C. T. Wang and Y. C. Hu, "Mixing of liquids using obstacles in Y-type microchannels," *Tamkang J. Sci. Eng.* **13**, 385–394 (2010).
- <sup>36</sup>M. Roudgar, E. Brunazzi, C. Galletti, and R. Mauri, "Numerical study of split T-micromixers," *Chem. Eng. Technol.* **35**, 1291–1299 (2012).
- <sup>37</sup>S.-S. Hsieh, J.-W. Lin, and J.-H. Chen, "Mixing efficiency of Y-type micromixers with different angles," *Int. J. Heat Fluid Flow* **44**, 130–139 (2013).
- <sup>38</sup>W. Shih-Jeh, H. Hsiang-Chen, and F. Wen-Jui, "Novel design and fabrication of a geometrical obstacle-embedded micromixer with notched wall," *Jpn. J. Appl. Phys., Part 1* **53**, 097201 (2014).
- <sup>39</sup>A.-S. Yang, F.-C. Chuang, C.-K. Chen, M.-H. Lee, S.-W. Chen, T.-L. Su, and Y.-C. Yang, "A high-performance micromixer using three-dimensional Tesla structures for bio-applications," *Chem. Eng. J.* **263**, 444–451 (2015).
- <sup>40</sup>P. M. Ligrani and R. D. Niver, "Flow visualization of Dean vortices in a curved channel with 40 to 1 aspect ratio," *Phys. Fluids* **31**, 3605 (1988).
- <sup>41</sup>S. A. Berger, L. Talbot, and L. S. Yao, "Flow in curved pipes," *Annu. Rev. Fluid Mech.* **15**, 461–512 (1983).
- <sup>42</sup>S. Hardt and F. Schönfeld, "Laminar mixing in different interdigital micromixers: II. Numerical simulations," *AIChE J.* **49**, 578–584 (2003).
- <sup>43</sup>L. L. Fan, X. L. Zhu, H. Zhao, J. Zhe, and L. Zhao, "Rapid microfluidic mixer utilizing sharp corner structures," *Microfluidics Nanofluidics* **21**, 36 (2017).
- <sup>44</sup>A. P. Sudarsan and V. M. Ugaz, "Fluid mixing in planar spiral microchannels," *Lab Chip* **6**, 74–82 (2006).
- <sup>45</sup>M. C. Liu, "Integrated microfluidic devices for cell culture and assay," Ph.D. thesis, California Institute of Technology, Pasadena, California, USA, 2010.
- <sup>46</sup>A. Papaioannou, S. Morin, A. M. Cheung, S. Atkinson, J. P. Brown, S. Feldman, D. A. Hanley, A. Hodsman, S. A. Jamal, S. M. Kaiser, B. Kvern, K. Siminoski, and W. D. Leslie, "2010 clinical practice guidelines for the diagnosis and management of osteoporosis in Canada: Summary," *Cmaj* **182**, 1864–1873 (2010).
- <sup>47</sup>C. Cadart, L. Venkova, P. Recho, M. C. Lagomarsino, and M. Piel, "The physics of cell-size regulation across timescales," *Nat. Phys.* **15**, 993–1004 (2019).